Submitted to the Int Journal of Materials Science and Engineering, March 2011

Time-Dependent Deformation of Low Carbon Steel at Elevated Temperatures

Kimberly Maciejewski[1], Yaofeng Sun[1], Otto Gregory[2] and Hamouda Ghonem[1]

[1]Department of Mechanical Engineering and Applied Mechanics, [2]Department of Chemical Engineering, University of Rhode Island, Kingston, R.I. 02881, U.S.A.

Abstract

This paper focuses on the microstructure and deformation properties of structural steel at elevated temperatures. The amounts and morphology of carbides present were monitored as a function of thermal exposure parameters. It was observed that as the temperature approaches the ferrite-austenite phase transformation (727°C), considerable diffusion of cementite plates and abnormal grain growth occurs. A viscoplastic constitutive model has been employed to simulate the flow behavior of the steel. Monotonic and cyclic tests were carried out to determine the kinematic and isotropic hardening parameters required for full identification of the model variables. Results of the model were compared with those obtained experimentally. The material parameters were shown to be sensitive to the microstructure and temperature. Variation in carbide amounts and morphology in the post thermal exposed specimens result in differences in the kinematic hardening, as compared to the as received material. Furthermore, the temperature sensitivity of the isotropic hardening is indicated by the presence a cyclic hardening/ softening transition in the temperatures 600°C - 700°C. Validity of the model in capturing time dependent behavior of the structural steel is examined using a sequentially coupled thermal-stress finite element analysis of single steel beam. Results of this simulation are discussed in terms of effects of temperature and strain-rate sensitivity on the material's viscoplastic deformation response.

Keywords: Low Carbon Steel, Structural Steel, Non Linear Kinematic Hardening, Strain Rate Sensitivity, Microstructure, High Temperature, Finite Element

1. Introduction

Accurate characterization and simulation of the deformation response of structural steel is an important concern in establishing a damage criterion for the design of civil structures. In general, design requirements to resist thermal exposures resulting from direct fire are thought of in the context of life safety and not in terms of life-cycle performance. On the other hand, post-thermal exposure performance criteria for such structures may require serviceability and reuse. Under this condition, structure designs must be based on the ability of the structure to provide optimum fire resistance. This can be achieved through the utilization of the material plastic and viscoplastic response in a manner as to not compromise the integrity of the entire structure. The current state of knowledge concerning the deformation behavior of loaded structures focuses on the final state of the structure rather than the detailed knowledge of the transient effects leading

Biography: Kimberly Maciejewski (1984-), Female, Doctoral Candidate

to the progressive failure of the structure. The lack of this knowledge is due to the fact that failure events under thermal exposure are a highly coupled phenomenon. That depends in large on the mechanical and thermal properties of the reinforcing phase. In almost all existing critical facilities, and for years to come, structural low carbon steel is the prime reinforcing material. The variations in the loading rate associated with thermally exposed structure can alter the plastic flow characteristics of the steel. In addition, thermal exposure can reach temperature levels capable of introducing significant changes in the steel's microstructure and mechanical properties.

The mechanical behavior of various metals and alloys can be quite complex at high temperature where interactions of time- and temperature-dependent processes take place. The general approach to simulate steel response under fire conditions is the use of power law stress-strain equations [1]. Other studies [2] have modeled the deterioration in the material strength with increasing temperature by a set of nonlinear stress-strain-temperature relationships using a Ramberg-Osgood equation in which creep effects are implicitly included. This model includes the temperature dependent nonlinear material behavior, variations in temperature distributions both along and across each steel member within a structure, as well as, the effects of thermal strains and residual stresses. These types of strain-rate independent plasticity formulas, do not account for the interactive effects of plasticity and viscous flow, hardening or load rate sensitivity occurring under combined load and temperature environment, see for example, the work of Outinen et al. [3] on structural steel S355 and Makelainen et al. on high-strength structural steel S420M [1]. Another approach is the use of a continuously nonlinear stress-strain curves applied to subsegments with different temperatures. The average temperature of each subsegment is used to determine the appropriate stress-strain curve, and its average strain is used to find a tangent modulus from this curve. This approach, in addition to the requirement of a monotonic stress-strain database at varying temperatures and strain rates, is difficult to integrate within a complex structure [4]. Tan et al [5] have incorporated strain reversal into their modeling of steel structures, allowing one to analyze steel frames subjected to unloading or cooling of the structure. The program can analyze steel frames subjected either to increasing external loads at ambient temperature or constant external loads at elevated temperature. The factors affecting the structural behavior at elevated temperature include temperature-dependent material nonlinearity, geometric nonlinearity, thermal gradient, and the creep effect.

The work presented in this paper aims at describing the structural steel behavior under thermal exposure in terms of a unified flow formulation that takes into consideration the evolution of hardening features of the steel as a function of temperature and exposure time. These formulations, that couple the time dependent plastic response, are based on an internal state variable model incorporating kinematic and isotropic hardening variables. Thus, the model is capable of describing the material response under variable strain rate conditions. The first part of this paper explores the evolution of microstructure as a function of both time and temperature. This metallurgical study is aimed at investigating the amount and morphology of the iron carbide phase and grain size as a function of exposure time and temperature. Understanding these characteristics will lead to critical post thermal exposure conditions for mechanical testing. Mechanical tests carried out at post thermal and elevated temperatures for identification of the model parameters will be described in the second part of this paper. The third part of the paper will describe various numerical applications including, uniaxial simulations in one dimensional strain-controlled loading scenarios and a finite element model of a single beam exposed to varying temperature and loading scenarios.

2. Material Characterization

An important factor influencing time dependent deformation of the steel is the morphological changes in the grain size and carbides of the starting material. At temperatures in the range of 300-727°C, iron carbide can change from a plate-like habit or lamella (Fig. 1a), as in the case of pearlite, to a spherodized habit (Fig. 1b and 1c), depending on thermal exposure conditions. The microstructure of the as-received A572 grade 50 steel is typical of normalized steel, consisting of pearlite colonies and alpha-ferrite equiaxed grains, as seen in Fig. 1a. Evolution of microstructure was monitored as a function of temperature, ranging from 300°C to 700°C, and time, from 0 to 200 minutes. The upper temperature level was selected to be below the ferrite-austenite phase transformation temperature of 727°C, thus upon quenching the specimen, the microstructure will remain as a ferrite-cementite microstructure. The heat treatments were carried out in a vertical furnace followed by quenching in an ice salt water bath at the various exposure times. Microstructural features were evaluated using quantitative stereology techniques. The volumetric percent of pearlite was determined using computer software. The grain size was determined using the mean intercept method [6] and is reported as a mean intercept length.

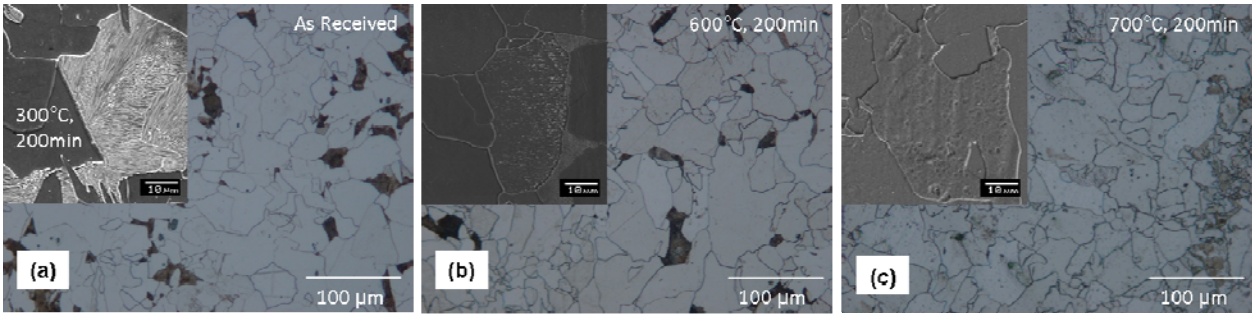

Figure 1: Micrographs of (a) as received low carbon steel and a specimen heat treated at 300°C, (b) 600°C and (c) 700°C for 200min. (All samples are etched for 5 seconds with 5 vol% nital)

The various thermal exposure conditions result in three basic microstructural conditions of carbide particles; pearlite colonies (Fig. 1a and 1b), spherodized particles of carbon (Fig. 1b and 1c), and absence of pearlite colonies (Fig. 1c). Analysis of the 700°C samples reveal the alpha-ferrite grains and almost no pearlite colonies, see Fig. 2a, while the amount of pearlite in samples exposed to temperatures 600°C and below did not notably vary from the as received condition. Fig. 2c shows that for the same temperature the exposure time does not have a significant effect in the amount of pearlite. Depending on time and temperature carbon particles go into solution, thus decreasing the amount of pearlite colonies present. Scanning electron microscopy was used to observe theses grains at a higher magnification as shown in Fig. 1b and 1c. Some grains heat treated at 600°C and 700°C showed evidence of spherodization.

The heat treatments have not shown significant grain growth at temperature exposures below 600°C, as seen in Fig. 2b. The average for 300°C, 500°C, and 600°C is fairly steady around about 50 µm. There is a slight increase in grain size for the longer exposure times for the 700°C sample. These results are consistent with those observed by Gayle et al, which did not see microstructural changes at or below 500°C [7]. Fig. 2d shows that for temperatures below 600°C, exposure time had no significant effect on grain size. At 700°C, the average grain size increased

with exposure time. The 600°C and 700°C specimens also show evidence of a bimodal distribution which generally results from the pinning of grain boundaries by impurities thus preventing diffusion across boundaries [8, 9].

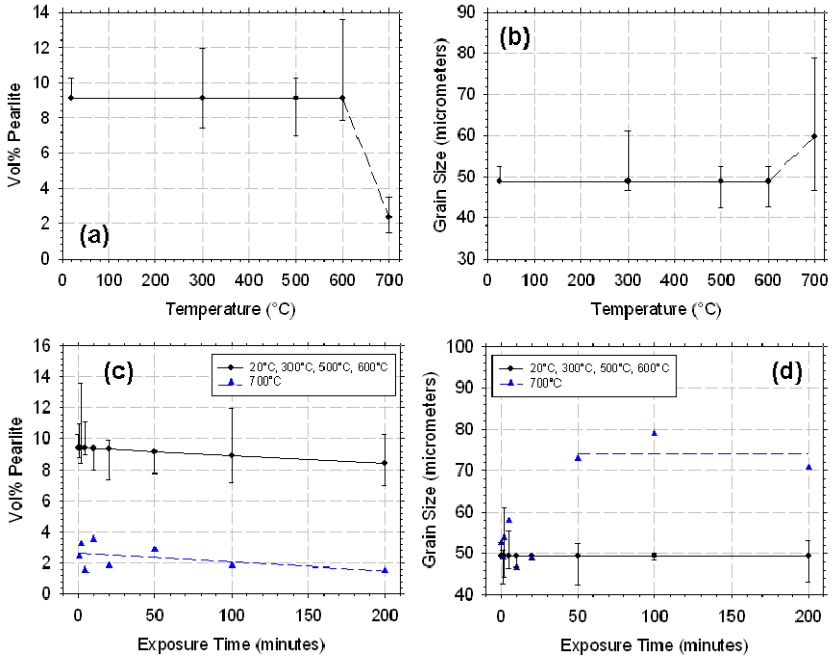

Figure 2: The effects of temperature and time on volume percent pearlite and grain size. (a) Temperature vs. volume percent pearlite, (b) temperature vs. grain size, (c) exposure time vs. volume percent pearlite, and (d) exposure time vs. grain size.

The thermal exposures can be grouped into three categories. The as received, 300°C and 500°C, represent the condition of equiaxed grains with pearlite colonies. The 700°C shows spherodized particles of carbon with the absence of pearlite colonies and a bimodal grain size. The third category, 600°C, shows transitional characteristics, with pearlite colonies and evidence of spherodization. As a result, the heat treatments selected for mechanical testing were, as received, 600°C and 700°C.

3. Non-Linear Kinematic Hardening Model

Different unified material constitutive models, that exist in literature, have the ability to account for the combined effects of plastic and creep deformation response of a microstructure, see work by Bodner Partom, Miller, Chaboche, Voyjadis [10, 11]. These models, generally, include terms that account for the evolution of isotropic and kinematic hardening parameters during the loading history of the material. The model selected here is the one developed by Chaboche and Rousselier [12, 13]. The attraction of this model, in addition to fact that it requires the determination of a limited number of material variables, is its inclusion of explicit hardening terms that account for deformation recovery and thus capable of modeling the strain-rate sensitivity of the material. The model is formulated on the assumption that a viscoplastic potential, Ω, exists in the stress space. A particular form of the viscoplastic potential is given in equation (1) [14].

$$\Omega = \frac{K}{\alpha(n+1)} \exp\left(\alpha \left\langle \frac{\sigma_v}{K} \right\rangle^{n+1} \right) \tag{1}$$

Where K, n, and α are material parameters that characterize the rate sensitivity. To describe the viscoplastic behavior, the concept of time-dependent overstress or viscous stress is used. This is given as:

$$\sigma_v = |\sigma - X| - R - k \tag{2}$$

The variable σ signifies the applied stress tensor and k is a temperature dependent material constant representing the initial size of the elastic domain. R and X are hardening variables corresponding to isotropic stress or drag stress and kinematic stress or back stress tensor. $J(\sigma - X)$ is Von Mises second invariant and σ' and X' are the deviatoric parts of σ and X respectively. The relation between plastic flow and the viscoplastic potential is determined by means of the normality rule to give equation (3) [12, 13, and 15].

$$\dot{\varepsilon}_p = \left\langle \frac{\sigma_v}{K} \right\rangle^n \exp\left(\alpha \left\langle \frac{\sigma_v}{K} \right\rangle^{n+1} \right) sign(\sigma - X) \tag{3}$$

The rules governing the evolution of the kinematic and the isotropic hardening variables are described below. Here it should be mentioned that the low carbon steel under consideration, as will be detailed later, exhibits strain rate sensitivity which is important in loading scenarios involving variable force distributions arising from thermal distributions [16]. As such, it is necessary to incorporate recovery terms into the hardening laws. The kinematic hardening term, measured by the back stress X, is expressed as a sum of a linear, X_2, and non-linear, X_1, time-dependent term, as shown in equation (4) [17, 18]. Equations (5) and (6) are general forms of back stress including strain hardening, dynamic recovery and static recovery terms [14, 19, and 20].

$$X = X_1 + X_2 \tag{4}$$

$$\dot{X}_1 = C_1(a_1\dot{\varepsilon}_p - X_1|\dot{\varepsilon}_p|) - \beta_1 |X_1|^{r_1 - 1} X_1 \tag{5}$$

$$\dot{X}_2 = C_2(a_2\dot{\varepsilon}_p - X_2|\dot{\varepsilon}_p|) - \beta_2 |X_2|^{r_2 - 1} X_2 \tag{6}$$

Where C, a, β, and r are material-dependent parameters.

The slow evolution of microstructure associated with cyclic hardening or softening of the material can be described by the isotropic hardening variable, R, which is the difference in the saturation position after a loading cycle and that corresponding to the monotonic loading for the same plastic strain. This is governed by the following equations (7), (8), and (9).

$$\dot{R} = b(Q - R)|\dot{\varepsilon}_p| \tag{7}$$

$$Q = Q_{max}\left(1 - e^{-\mu q}\right) \tag{8}$$

$$q = \max(|\varepsilon_p|, q) \tag{9}$$

Where Q and b are the limiting values of the isotropic hardening variable. Q is the saturation limit of R, while the constant, b, is a temperature and material-dependent parameter describing how fast R reaches Q. This latter parameter can be either a positive value, indicating cyclic hardening, or a negative value, indicating cyclic softening. Q_{max} is the maximum value of Q, and q is the maximum strain achieved during loading, which memorizes the previous plastic strain range [21].

4. Experimental Determination of Model Constants

A series of strain-controlled tests were carried out on A572 Grade 50 Low Carbon Steel, at both room and high temperature, to determine the various material parameters described above in order to fully identify the non-linear kinematic hardening model. The mechanical testing was carried out using a servo hydraulic test machine, equip with a heat induction coil for the high temperature tests. The strain was measured with a quartz rod extensometer. A monotonic test is carried out, at a strain rate of $5x10^{-6}$ sec^{-1}, to determine the modulus, E, and yield stress, k, of the material. Results of this rate at various loading conditions are shown in Fig. 3a-3c and Fig. 4a.

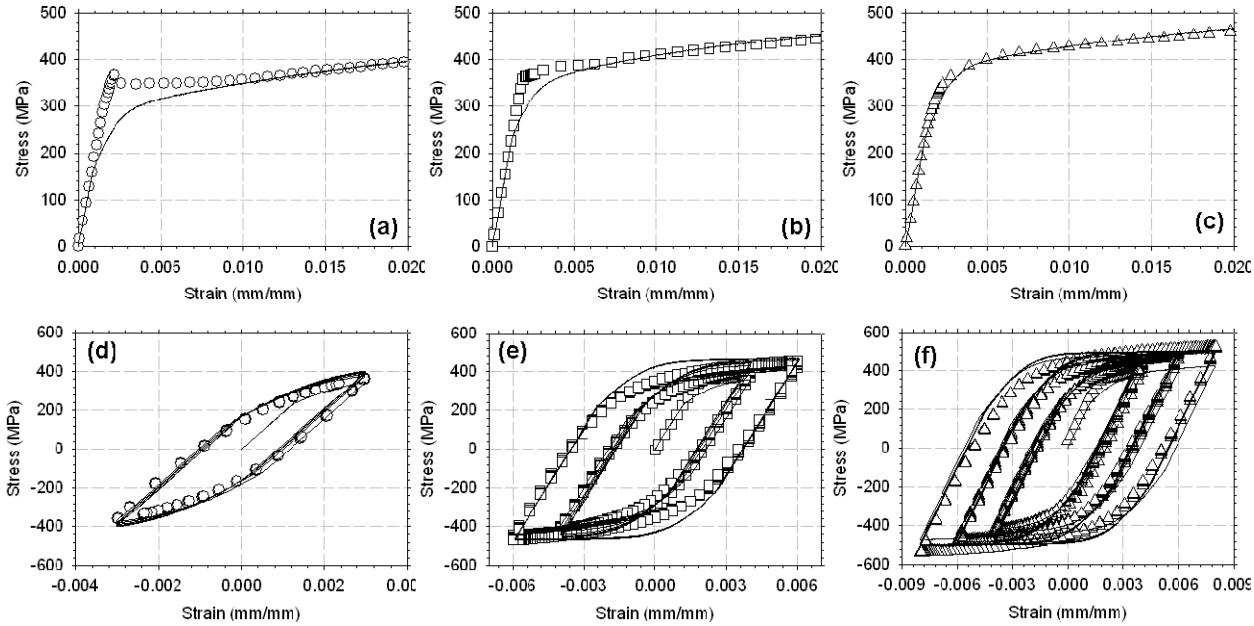

Figure 3: Comparison between experimental (Symbol) and numerical (Solid line) monotonic stress-strain curves for (a) as received, (b) post-600°C thermal exposure, and (c) post-700°C thermal exposure low carbon steel tested at room temperature. Comparison between experimental and numerical cyclic stress-strain loops at various strain ranges for low carbon steel for the following test conditions at room temperature, (d) as received, (e) post-600°C thermal exposure, (f) post-700°C thermal exposure

A series of strain-controlled fully reversed cyclic stress-strain tests (R=-1) are performed, until peak stress saturation is reached, at a strain rate of $5x10^{-6}$ sec^{-1}. The strain range of these tests varied from ±0.2% to ±1% strain. The cyclic stress-strain curves at various test conditions are shown in Fig. 3d-3f and Fig. 4b-4c. These loops are employed to generate the isotropic and kinematic hardening, as well as, viscosity and recovery parameters, which are described below.

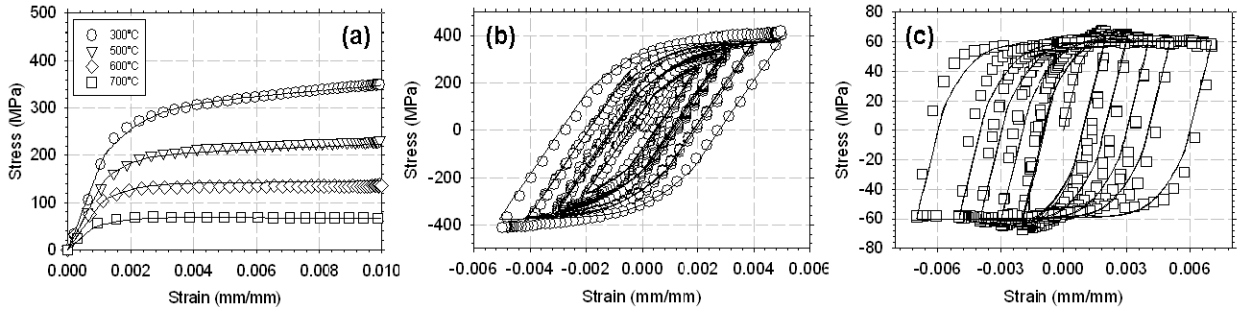

Figure 4: Comparison between experimental (Symbol) and numerical (Solid line) monotonic stress-strain curves for (a) as received tested at high temperatures. Comparison between experimental and numerical cyclic stress-strain loops at various strain ranges for as received low carbon steel tested at (b) 300°C and (c) 700°C.

Isotropic Hardening Parameters: The slow internal changes described by isotropic stress occurs over a large number of cycles and is a function of accumulated plastic strain, corresponding to the difference in the maximum stress of the current cycle and the maximum stress of the first loop associated with the monotonic stress-strain curve. Assuming the increase in maximum stress, σ_M, occurs only due to isotropic hardening, R, the following relationship can be determined, see Nouailhas [14, 22]:

$$\frac{R}{Q} = \frac{\sigma_M - \sigma_{M0}}{\sigma_{MS} - \sigma_{M0}} = (1 - e^{-bp}) \tag{10}$$

Where σ_M, σ_{MS}, σ_{M0} correspond to the maximum stress of cycle M, the maximum stress of the saturated cyclic loop and the first loop respectively. The accumulated plastic strain, p, is defined by $p = \left|\varepsilon_p\right| = 2N\Delta\varepsilon_p$. N is the number of cycles and ε_p is the sum of plastic strain in tension and compression. The material parameter, b, is determined by fitting of the above equation to the experimental R/Q vs. p data as shown below in Fig. 5a for high temperature test conditions at 300°C.

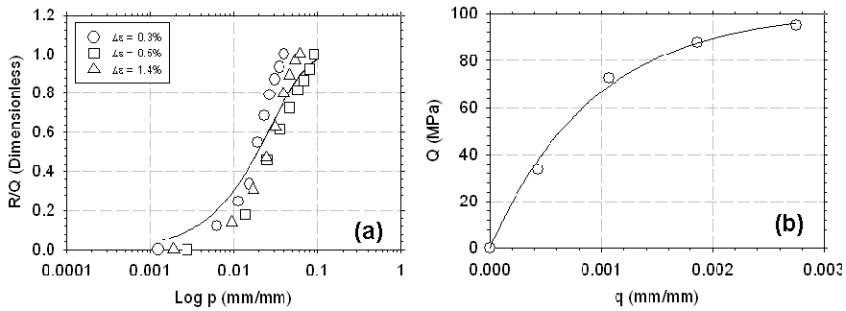

Figure 5: (a) Fit of equation (10) (Solid line) to experimental (Symbol) R/Q vs. log accumulated plastic strain for low carbon steel for at 300°C. (b) Fit of equation (8) (Solid line) to experimental (Symbol) Q vs. q for low carbon steel for at 300°C.

Q_{max} and μ are calculated by fitting of the equation (8) to the experimental Q vs. q data as shown in Fig. 5b. Where $Q_{max} = \sigma_{MS} - \sigma_{M0}$ and q is the maximum strain achieved during loading, in this case $q = \Delta\varepsilon^p / 2$.

Kinematic Hardening Parameter: For each strain range, the hardening of the material in the first cycle of the cyclic stress-strain loops is assumed to be related to the kinematic hardening only and the accumulated plastic strain p is equal to the plastic strain ε_p. The kinematic stress corresponds to the center of the linear part of the first reversible cyclic loop at each strain range. As discussed earlier kinematic stress is expressed as the sum of two terms, each a function of plastic strain through integration of equations (5) and (6) X can be represented as follows:

$$X = a_1(1 - e^{-C_1\varepsilon_p}) + a_2(1 - e^{-C_2\varepsilon_p}) \tag{11}$$

Where a_i, the asymptotic value of X_i, and C_i, the rate at which X_i reaches a_i, are obtained from curve fitting of experimental X vs. ε_p data as shown below in Fig. 6.

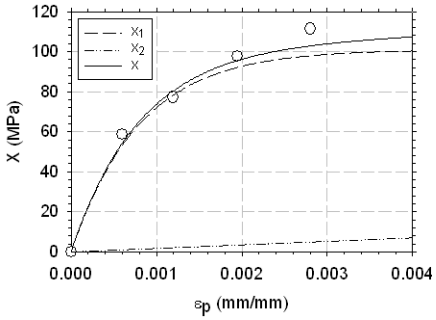

Figure 6: Fit of equation (11) (Lines) to experimental (Symbol) kinematic stress vs. plastic strain for low carbon steel at 300°C.

Viscous Stress Parameters: To describe the time-dependent viscous stress term, n and K, strain-rate sensitive parameters must be determined [14, 15, 23]. For this, a strain-controlled monotonic stress-relaxation test is performed. A typical relaxation test at 300°C is shown in Fig. 7a. During the periods of holding at a constant total strain, the stress as a function of time is acquired, as shown in Fig. 7b. Under constant strain conditions during hold time, the plastic strain rate can be written as $\dot{\varepsilon}_p = -\dot{\sigma}/E$. Where the stress rate is determined from the stress versus hold time graph shown in Fig. 7b and E is the modulus.

The viscous stress can be expressed in terms of plastic strain rate by rearranging the equation for plastic flow, given by equation (3), to the form:

$$\mathrm{Log}\left(\sigma - \sigma_i\right) = \frac{1}{\mathrm{n}}\mathrm{Log}\left(-\frac{\dot{\sigma}}{\mathrm{E}}\right) + \mathrm{LogK} \tag{12}$$

For arbitrary values of σ_i, one can plot log σ_v vs. log $\dot{\varepsilon}_p$. The parameters *n* and *K* are determined from fitting the linear part of the curve (Fig. 7c). An average of n and K is taken for different values of ε_t. The material constant, α, is taken to be the saturation limit of viscous stress for high plastic strain rates. This constant is determined by fitting equation (3) to the experimental viscous stress versus plastic strain rate in Fig. 8 at the highest plastic strain rate.

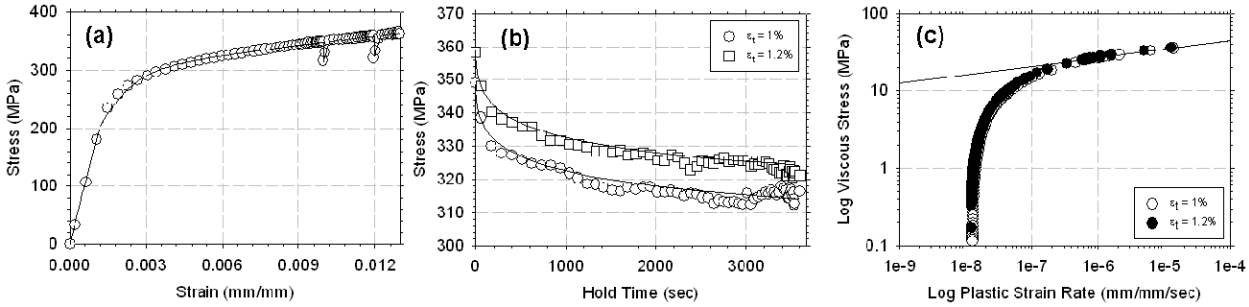

Figure 7: Comparison of experimental (Symbol) and numerical (Solid line) (a) relaxation stress vs. strain curve and (b) relaxation stress vs. hold time at constant strain values for low carbon steel at 300°C. (c) Fit of equation (13) (Solid line) to experimental (Symbol) log viscous stress vs. log plastic strain rate for low carbon steel at 300°C.

Recovery Parameters: Time-dependent recovery parameters, β_1, β_2, are determined from the linear portion of the stress time curve shown in Fig. 7b. The time dependent back stress can be expressed by rearranging equation (2) to the form:

$$X(t) = \sigma(t) - R - k - \sigma_v \tag{13}$$

Assuming that the stress time has a linear relationship, and the latter terms in equation (13) are constant, the above equation can be plotted as function of time and fit to equation (14) given below, where β_1, β_2, are determined. Equation (14) is determined through integration of equation (6) using a linear recovery term (assuming r = 1) yielding:

$$X(t) = \frac{C_1 a_1 \dot{p}}{C_1 \dot{p} + \beta_1}\left(1 - e^{-(C_1 \dot{p} + \beta_1)t}\right) + \frac{C_2 a_2 \dot{p}}{C_2 \dot{p} + \beta_2}\left(1 - e^{-(C_2 \dot{p} + \beta_2)t}\right) \tag{14}$$

These parameters, β_1, β_2, r_1, and r_2, are optimized with stress-strain data at various strain rates. Strain rate sensitivity tests [23] are performed in which a specimen is loaded monotonically in strain-control at multiple strain rates, as shown in Fig. 8.

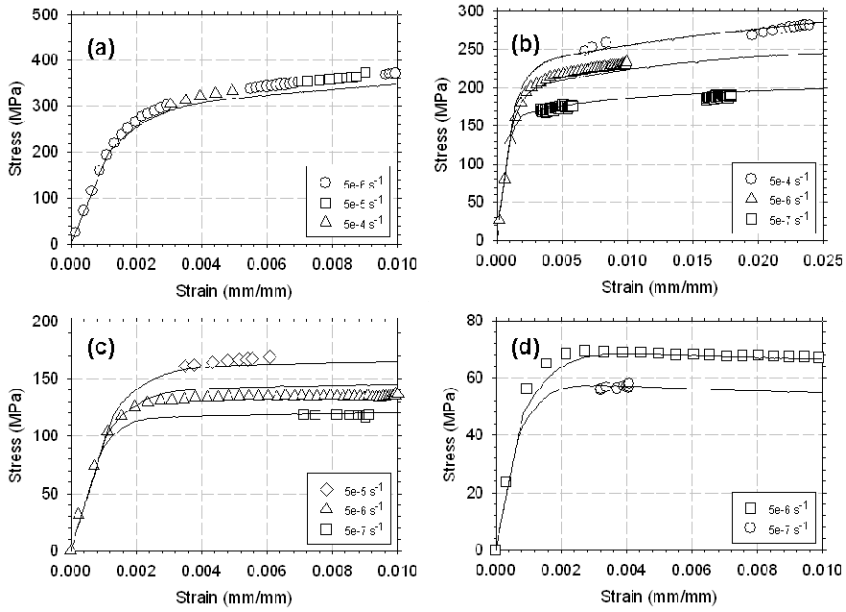

Figure 8: Comparison of experimental (Symbol) and numerical (Solid line) monotonic stress-strain curves at multiple strain rates for low carbon steel for the following test conditions at (a) 300°C, (b) 500°C, (c) 600°C, and (d) 700°C.

The material parameter determination procedure, described above, has been applied at two post-thermal exposure conditions, as well as, as received steel at temperatures ranging from 20-700°C.

5. Simulation and Validation of the Model

Modeling was achieved by carrying out a simultaneous integration of the set of viscoplastic constitutive equations described above. Monotonic strain-controlled loading at a rate of 5e-6s^{-1} case studies were performed and compared to those obtained experimentally as seen in Fig. 3a-c and Fig. 4a. The non linear kinematic hardening model is in good agreement with the experimental stress-strain curves. It is clear from this comparison that the model results are not capable of capturing the lüders phenomena with an upper and lower yield as seen in the experimentally obtained curves at room temperature conditions, see Fig. 3a. Furthermore, variations in the material constants for the mechanical testing at room temperature are detected in the asymptotic values of the kinematic hardening parameters, see Figs. 3b and 3c. These variations can be explained by the fact that the steel specimens that have been exposed to 700°C for 200 min microstructures revealed spherodization and almost no pearlite colonies. This

material would have more carbon solute atoms in the ferrite matrix, which would act as short range barriers for dislocations. This microstructure also revealed a bimodal grain size distribution, where the grain boundaries would act as long range barriers for dislocations which would in turn reflect on variations in the kinematic stress. In addition, Fig. 4a shows that at 700°C hardening decreases resulting in a perfectly plastic material.

Fully reversed strain-controlled loading case studies were simulated and compared to those obtained experimentally as shown in Fig. 3d-f and Fig. 4b-c. The peak stresses for all conditions agree well between the numerical and experimental curves. The plastic strain ranges agree better at lower temperature conditions than higher temperature conditions. Between the temperatures of 600°C and 700°C there is a transition between cyclic hardening and cyclic softening behavior as the sign of the Q_{max} parameter changes from positive to negative. This could be attributed to dissolution of pearlite colonies at 700°C; the lack of a hardening phase results in cyclic softening.

Case studies for monotonic strain-controlled loading at variable strain rates ranging from 5E-7 to 5E-4s^{-1} were performed and compared to those obtained experimentally as seen in Fig. 8. The model can illustrate both strain rate independent and dependent behavior. At 300°C the low carbon steel is strain rate independent. Above this temperature, the low carbon steel is increasingly strain rate sensitive. The recovery terms become more influential at higher temperatures. Generally for all cases, the non-linear kinematic hardening model is capable of modeling low carbon steel. It can not only capture the effects of variable loading, but also variable temperature conditions.

6. Applications

The one dimensional internal state variable (ISV) model previously described has been extended to a two dimensional UMAT subroutine, incorporating temperature-dependent material constants. These temperature-dependent constants consist of E, k, a_1, a_2, Q_{max}, K, α, β_1, and β_2. The formula used to fit the temperature-dependent material constants is given as:

$$C = A * TANH\left(-\left(T/T_0\right)^B\right) + C_0 \tag{15}$$

Where C and T represent a material constant and temperature respectively, A, B, T_0, and C_0, are unknown parameters which are figured out by curve fitting to C-T data.

This two dimensional model has been utilized to describe the combined effects of temperature and rate sensitivity on a single steel beam. The simulation of a single steel beam was performed using a commercial finite element program ABAQUS. The geometry models were built in ABAQUS/CAE. The two dimensional UMAT code for the ISV model was written and employed for the steel material. A single steel beam model, seen in Fig. 9, was built to illustrate effects of loading rate and temperature on the beam deflection. The two-dimensional beam is 3m long and 0.2m high. The elements are all plain strain elements. Each element has a size of 0.1m long, 0.02m high. The beam was fixed at both ends. Uniform temperature field was applied to the beam. Two temperature cases, 300°C and 700°C, were studied. Uniform pressure ramping up with time was also applied on the beam. Two study cases of pressure ramping rate were investigated. They are 1.5 MPa/min and 0.15 MPa/min. A combination of 2 temperature cases and 2 pressure ramping rates makes 4 simulation cases using single steel beam model.

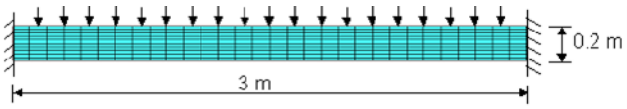

Figure 9: Single steel beam model.

Four simulation cases were run using the single steel beam model, and their beam deflections were output for comparative analysis. The four curves in Fig. 10 show the evolution of the maximum beam deflections along with the ramping pressure. Fig. 10a shows the beam deflections from 2 simulation cases at the same temperature of 300°C but at two different pressure ramping rates; Fig. 10b from another 2 simulation cases at the temperature 700°C. Low carbon steel exhibits both temperature and strain rate dependence. Fig. 10 emphasizes these dependencies. At elevated temperatures the strength increasingly degrades, as shown in Fig. 10c by the degradation of the peak stress. Fig. 10c also shows that the strain rate sensitivity increases with increasing temperature. Below a critical temperature, between 300°C and 500°C, the steel is rate-independent, while above this value, the steel is rate dependent. This shows the importance of a model which exhibits temperature and strain rate-dependencies.

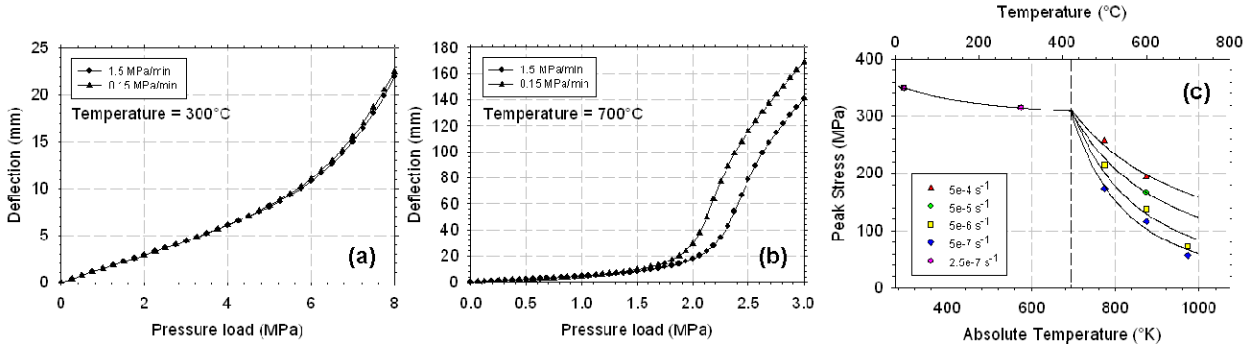

Figure 10: Beam deflection vs. pressure load at two loading rates at (a) 300°C and (b) 700°C. (c) Experimental (Symbol) and curve fit to an Arrhenius equation (Solid lines) of temperature and strain rate dependency of peak stress at a tensile strain 0.5%.

At the temperature 300°C (Fig. 10a), the beam deflection is not dependent on the pressure ramping rate, however it shows the dependence of pressure ramping rate at the temperature 700°C (Fig. 10b). The comparison accounts for the effect of strain-rate sensitivity on structural deformation. It is implied that 300°C is below the transition temperature of the material strain-rate sensitivity, and 700°C is above that (as implied by Fig. 10c). If we compare the beam deflections under the same pressure load but at the two different temperatures, it is obvious that the beam deflection is larger at the higher temperature 700°C. The higher temperature reduces the strength of the material steel or the stiffness of the steel beam.

7. Summary and Conclusions

The work in this paper has examined the microstructure variations and deformation response of structural steel A572 grade 50 steel at elevated temperatures. Changes in the grain size as well as amounts and morphology of carbides present were monitored as a function of temperature, ranging from room temperatures up to 700°C for exposure times up to 200 minutes. Furthermore, a viscoplastic constitutive model has been employed to simulate the flow behavior of the steel in the temperature ranges mentioned above and a series of monotonic and cyclic tests

were carried out to determine the parameters required for full identification of the model variables. The main conclusions of this study can be summarized as follows:

1. The grain size, measuring 50 μm, did not show changes for all thermal exposure conditions below 600°C. The 600°C and 700°C specimens show evidence of a bimodal distribution. The as received material and those that have been heat treated at temperatures 600°C and below, show no changes in the amount of pearlite colonies present while the condition at 700°C shows the absence of pearlite colonies. In addition, spherodized particles of carbon have been observed at specimens exposed to 600°C and 700°C.
2. An Internal State Variable model, incorporating temperature-dependent material constants, static and dynamic recovery terms, based on non-linear kinematic hardening formulations to describe the viscoplastic flow behavior of low carbon structural steel under variable thermal conditions has been examined. Validity of the fully formulated constitutive model has been established through comparison with corresponding experimental results.
3. Monotonic and cyclic tests were performed at both room temperature and high temperature in order to provide data to determine material dependent parameters for a non-linear kinematic hardening model. The material parameters are shown to be not only responsive to variations in temperature, but microstructure as well. Microstructure sensitivity is seen through differences in the kinematic hardening for the mechanical testing at room temperature which suggest that the spherodized carbide particles and bimodal grain size distribution in the post thermal exposed specimens act as barriers for dislocations. Furthermore, between the temperatures of 600°C and 700°C there is a transition between cyclic hardening and cyclic softening behavior, thus indicating the temperature sensitivity of the isotropic hardening.
4. The temperature and rate sensitivity of low carbon steel has been examined using a finite element analysis of a steel-beam. This has been implemented with a sequentially coupled thermal-stress analysis under variable loading and temperature scenarios. The predicted deformation shows that it is necessary to consider the time-dependent plastic deformation in the steel-beam subjected to elevated temperature.

Acknowledgments

This work has been supported by FM Global and the Department of Homeland Security Center of Excellence: Explosives Detection, Mitigation, and Response at the University of Rhode Island

References:

[1] Makelainen P, Outinen J, Kesti J., Fire design model for structural steel S420M based upon transient-state tensile test results [J], Journal of Constructional Steel Research, 1998, 48, 47-57.

[2] Saab, H.A., and Nethercot, D.A., Modelling Steel Frame Behavior Under Fire Conditions [J], Engineering Structures, 1991, 13, 371-382.

[3] Outinen J, Kesti J, Makelainen, P., Fire Design Model for Structural Steel S355 Based Upon Transient State Tensile Test Results [J], Journal of Constructional Steel Research, 1997, 42 (3), 161-9.
[4] Najjar, S.R., and Burgess, I.W., A Nonlinear Analysis for Three-Dimensional Steel Frames in Fire Conditions [J], Engineering Structures, 1996, 18 (1), 77-89.
[5] Tan, K.H., Ting, S.K., and Huang, Z.F., Visco-Elasto-Plastic Analysis of Steel Frames in Fire [J], Journal of Structural Engineering, 2002, 128 (1), 105-114.
[6] Vander Voort, George F., Metallography Principles and Practice [M], New York, USA: McGraw-Hill, 1984.
[7] Gayle, Frank W., Fields, Richard J., Luecke, William E., Banovic, Stephen W., Foecke, Timothy, McCowan, Christopher N., McColskey, J. David, and Siewert, Thomas A., Mechanical and Metallurgical Analysis of Structural Steel [R], NIST NCSTAR 1-3, Federal Building and Fire Safety Investigation of the World Trade Center Disaster, September, 2005.
[8] Callister, William. D, Jr., Materials Science and Engineering an Introduction [M], Seventh Edition, York, PA., USA: John Wiley and Sons, Inc., 2007.
[9] Dieter, George E., Mechanical Metallurgy [M], USA: McGraw-Hill, 1986.
[10] Stouffer, Donald C., and Dame, L. Thomas, Inelastic Deformation of Metals Models, Mechanical Properties, and Metallurgy [M], New York: John Wiley and Sons, Inc., 1996.
[11] Yaguchi, Masatsugu, and Takahashi, Yukio, Unified Inelastic Constitutive Model for Modified 9Cr-1Mo Steel Incorporating Dynamic Strain Aging Effect [J], JSME International Journal Series A, 1999, 42(1).
[12] Chaboche, J.L., and Rousselier, G., On the Plastic and Viscoplastic Constitutive Equations—Part I: Ruled Developed with Integral Variable Concept [J], Transactions of the ASME, Journal of Pressure Vessel Technology, 1983, 105, 123-133.
[13] Chaboche, J.L., and Rousselier, G., On the Plastic and Viscoplastic Constitutive Equations—Part II: Application of Integral Variable Concepts to the 316 Stainless Steel [J], Transactions of the ASME, Journal of Pressure Vessel Technology, 1983, 105, 159-164.
[14] Nouailhas, D., Unified Modeling of Cyclic Viscoplasticity: Application to Austenitic Stainless Steels [J], International Journal of Plasticity, 1989, 5, 501-520.
[15] Chaboche, J.L., Constitutive Equations for Cyclic Plasticity and Cyclic Viscoplasticity [J], International Journal of Plasticity, 1989, 5, 247-302.
[16] Wang, Y.C., Lennon, T., and Moore, D.B., The Behavior of Steel Frames Subject to Fire [J], Journal of Constructional Steel Research, 1995, 35, 291-322.
[17] Chaboche, J.L., Dang Van, K., and Cordier, G., Modelization of the Strain Memory Effect on the Cyclic Hardening of 316 Stainless Steel [C], Proceedings of the Fifth International Conference on SMIRT, Div. L, Berlin, Germany, 1979.
[18] Chaboche, J.L., On Some Modifications of Kinematic Hardening to Improve the Description of Ratchetting Effects [J], International Journal of Plasticity, 1991, 7, 661-678.
[19] Prager, W., Recent Developments in the Mathematical Theory of Plasticity [J], Journal of Applied Physics, 1949, 20(3), 235-241.
[20] Armstrong, P.J., and Frederick, C.O., A Mathematical Representation of the Multiaxial Bauschinger Effect [R], Berkeley Nuclear Laboratories, Report RD/B/N731, 1996.
[21] Zaki, A.S., and Ghonem, H., Modeling the Ratcheting Phenomenon in an Austenitic Steel at Room Temperature [C], Proceeding of the ASME 2000 Design, Reliability, Stress

Analysis and Failure Prevention Conference, Sept. 10-13, Baltimore, Maryland, USA, 2000.
[22] Nouailhas, D., A Viscoplastic Modelling Applied to Stainless Steel Behavior [C], Proceedings of the Second International Conference on Constitutive Laws for Engineering Materials: Theory and Application, January 5-8, Tuscon, Arizona, USA, 1987, 717-724.
[23] Lemaitre, J., and Chaboche, J.L., Mechanics of Solid Materials [M], Cambridge, United Kingdom: Cambridge University Press, 1990.